

Identification of stable alloy with giant magnetization via machine learning based autonomous materials search

Yuma Iwasaki (✉ iwasakiyuma@nec.com)

NEC (Japan)

Ryohto Sawada

Eiji Saitoh

Masahiko Ishida

Article

Keywords: Fe₃Co₁, alloys, magnetization

Posted Date: August 14th, 2020

DOI: <https://doi.org/10.21203/rs.3.rs-55136/v1>

License: © ⓘ This work is licensed under a Creative Commons Attribution 4.0 International License.

[Read Full License](#)

Version of Record: A version of this preprint was published at Communications Materials on March 19th, 2021. See the published version at <https://doi.org/10.1038/s43246-021-00135-0>.

1 Identification of stable alloy with giant magnetization via 2 machine learning based autonomous materials search.

3
4 Yuma Iwasaki^{1,2,3*}, Ryohto Sawada¹, Eiji Saitoh^{4,5,6,7,8} & Masahiko Ishida^{1,3}

5
6 ¹*System Platform Research Laboratories, NEC Corporation, Kawasaki 211-8666, Japan*

7 ²*PRESTO, JST, Saitama 322-0012, Japan*

8 ³*NEC-AIST Quantum Technology Cooperative Research Laboratory, National Institute of Advanced Industrial
9 Science and Technology (AIST), Tsukuba, 305-8568, Japan*

10 ⁴*Institute for Materials Research, Tohoku University, Sendai 908-8577, Japan*

11 ⁵*Center for Spintronics Research Network, Tohoku University, Sendai 980-8577, Japan*

12 ⁶*Department of Applied Physics, University of Tokyo, Tokyo 113-8656, Japan*

13 ⁷*Advanced Institute for Materials Research, Tohoku University, Sendai 908-8577, Japan*

14 ⁸*Advanced Science Research Center, Japan Atomic Energy Agency, Tokai, 319-1195, Japan*

15 Email: y-iwasaki@ih.jp.nec.com

1 **Discovery of new magnets with high magnetization has always been important in human history**
2 **because it has given birth to powerful motors and memory devices. Currently, the binary alloy Fe_3Co_1**
3 **exhibits the largest magnetization of any stable alloys explained by the Slater-Pauling rule. A multi-**
4 **element alloy system has been expected to include an alloy with magnetization beyond that of Fe_3Co_1 ,**
5 **but it has been difficult to identify appropriate elements and compositions because of combinatorial**
6 **explosion in the multi-element system. In this work, we found a new alloy with giant magnetization**
7 **beyond that of Fe_3Co_1 via an autonomous materials search system combining machine learning and ab-**
8 **initio calculation. After autonomous/automated exploration in the large material space of multi-element**
9 **alloy for six weeks, the system unexpectedly indicated that Ir and/or Pt impurities would enhance the**
10 **magnetization of FeCo alloys. To confirm this experimentally, we comprehensively synthesized**
11 **$\text{Fe}_x\text{Co}_y\text{Ir}_{1-x-y}$ and $\text{Fe}_x\text{Co}_y\text{Pt}_{1-x-y}$ alloys and found that some of them have magnetization beyond that of**
12 **Fe_3Co_1 .**

13 Materials with a high magnetization are indispensable for information storages, motors, sensors,
14 actuators, and other electric devices^{1,2}. The metastable iron nitride $\alpha''\text{-Fe}_{16}\text{N}_2$ is believed to have the highest
15 magnetization³. However, it decomposes at a relatively low temperature ($\sim 250\text{ }^\circ\text{C}$), and this thermal instability
16 precludes practical application of the material⁴. Some of metastable alloys, where the crystal structure and lattice
17 constant are fixed by force, also exhibit the high magnetization. For instance, ultrathin epitaxial films of
18 $\text{Fe}_x\text{Co}_y\text{Mn}_z$ have very high magnetization, but it was not achieved in stable states such as a non-epitaxial film
19 and bulk⁵. Therefore, a stable alloy with a high magnetization has been desired for practical applications. As
20 shown by the Slater–Pauling curve (Supplementary Fig. S1), the binary alloy $\text{Fe}_{75}\text{Co}_{25}$ (= Fe_3Co_1) has the

1 highest magnetization of any alloy⁶. Generations of scientists have tried to discover a stable magnetic alloy
2 beyond the Fe₃Co₁ limit by investigating multi-element alloys, but it is difficult to study multi-element alloys
3 comprehensively because we have to carry out a quite large number of simulations and/or experiments due to
4 combinatorial explosion.

5 Multi-element materials are often investigated by machine learning, which is used because of its ability
6 for multi-dimensional analysis⁷⁻¹⁷. It is noteworthy that ML has already been used to develop materials for
7 magnets^{18,19}, batteries^{20,21}, superconductors^{22,23}, ferroelectrics^{24,25}, thermoelectrics^{26,27} and photovoltaics^{28,29}.
8 Data-driven ML approaches should shed new light on our knowledge of materials and thus bring about the
9 discovery of unexpected novel materials.

10 Sumita et al.³⁰ and Sawada et al.³¹ have recently suggested an autonomous materials search system
11 that simulates the entire process of conventional manual materials search shown in Fig. 1a: (A) fabricate
12 materials, (B) evaluate their properties, and (C) decide on next target materials. Figure 1b shows the
13 autonomous materials search system combining ML and ab-initio simulation technologies. The virtual materials
14 fabrication step (A') and virtual materials evaluation step (B') are simulated using the *ab-initio* method, which
15 predicts various material properties from the composition and crystal structure information. For the step deciding
16 the next target composition/structure (C'), ML techniques such as Bayesian optimization³⁰ and game tree
17 search³¹ are used. ML is used to decide the next target material from the data obtained in step B', with
18 consideration of the trade-off between exploration and exploitation (i.e., these ML techniques are adjusted to
19 select a next target material with a better property from materials dissimilar to those that have already been tried
20 in steps A' and B'). Since the amount of learning data increases with repetition of this automated cycle, the ML

1 model gradually improves and suggests better materials.

2 **Results**

3 In the work presented here we used the autonomous materials search system to identify a multi-
4 element alloy with high magnetization. To find a potential high-magnetization alloy, the autonomous system was
5 set to the task of optimizing the composition of a disordered multi-element alloy ($\text{Fe}_a\text{Co}_b\text{Ni}_c\text{Ru}_d\text{Rh}_e\text{Pd}_f\text{Ir}_g\text{Pt}_h$) with
6 a body-centred cubic (bcc) crystal structure. The settings, including the selection of elements and structure, were
7 determined by a simple pre-simulation (see Methods section and Supplementary Fig. S2). We used the
8 Korringa–Kohn–Rostoker coherent potential approximation (KKR-CPA) method for the *ab-initio* simulation parts
9 (A' and B') due to its good agreement with experimental results, especially in disordered multi-element alloy
10 systems³²⁻³⁵. The magnetic moment, which is roughly proportional to magnetization, was calculated using the
11 KKR-CPA and the calculated composition values (a, b, c, d, e, f, g and h) decided by the ML part (C') using the
12 game tree algorithm³¹. Details of the algorithms and their parameters can be found in the Methods section.

13 We ran the autonomous system for nine weeks. The growth progress is illustrated in Fig. 2, where the
14 magnetic moment data are plotted per cycle shown in Fig. 1b. Over time, as the available learning data
15 increased, the system was able to suggest compositions for alloys with larger magnetic moments. It is
16 particularly noteworthy that the autonomous system sometimes tested material compositions with small
17 magnetic moments, clearly demonstrating that it considered both exploration and exploitation during the multi-
18 dimensional virtual search. Some low-score data were necessary for the global optimization process because
19 diversity (dispersion) of the learning data is essential for constructing a good ML (game tree) model.

1 The red line in Fig. 2 shows the maximum magnetic moment at each point in time. Eventually, after six
2 weeks of growth, an alloy with the largest magnetic moment was suggested: $\text{Fe}_{82}\text{Co}_{13}\text{Ir}_4\text{Pt}_1$. It is only reasonable
3 that Fe and Co are its main components because $\text{Fe}_{75}\text{Co}_{25}$ is the known alloy with the largest magnetic moment.
4 However, the presence of Ir and Pt impurities in the material is seemingly inconsistent with chemical intuition
5 because both elements have small magnetic moments, which would be expected to reduce the magnetic
6 moment of the alloy. In other words, the autonomous materials search system suggested an unexpected novel
7 alloy with high magnetization.

8 To confirm the effect of Ir and Pt impurities experimentally, we synthesized $\text{Fe}_x\text{Co}_y\text{Ir}_{100-x-y}$ and
9 $\text{Fe}_x\text{Co}_y\text{Pt}_{100-x-y}$ ternary alloys and evaluated their magnetization. For comparison, the ternary alloy $\text{Fe}_x\text{Co}_y\text{Ni}_{100-x-y}$
10 was also investigated because Ni is the element with the third largest magnetic moment (after Fe and Co). To
11 investigate the composition dependency within the ternary alloys, we have carried out combinatorial
12 experiments^{36,37} using composition-spread thin films on SiO_2/Si , each mapping a large fraction of the alloy's
13 composition range on one library wafer. Figure 3a shows the conceptual image of combinatorial sputtering,
14 where the use of three sputter guns and an automated moving mask enables synthesis of a linear composition-
15 spread thin film³⁶⁻³⁸. Figure 3b shows the composition map of an $\text{Fe}_x\text{Co}_y\text{Ir}_{100-x-y}$ composition-spread thin film. For
16 sampling points shown as many black spots in Fig. 3b, we carried out combinatorial longitudinal magneto-optic
17 Kerr effect (combi-MOKE)³⁹ experiments. Figure 3c shows the results of combi-MOKE experiments with
18 $\text{Fe}_x\text{Co}_y\text{Ir}_{100-x-y}$ composition-spread samples. As an example, Fig. 3d shows the MOKE curves of $\text{Fe}_{68.1}\text{Co}_{26.2}\text{Ir}_{5.7}$
19 (bottom right point in Fig. 3b). Note that the vertical axis value in Fig. 3d is normalized by the maximum MOKE

intensity of pure Fe (top left point in Fig. 3b). The amplitude of a MOKE curve is proportional to saturation magnetization M_s ⁴⁰:

$$M_s \propto M_{MOKE} = \frac{I_{max}^{MOKE} - I_{min}^{MOKE}}{2},$$

where M_{MOKE} is the amplitude of the MOKE curve and I_{max}^{MOKE} and I_{min}^{MOKE} are respectively the maximum and minimum values of the normalized MOKE intensity. As with the $Fe_xCo_yIr_{100-x-y}$ composition-spread thin film, we also fabricated $Fe_xCo_yPt_{100-x-y}$ and $Fe_xCo_yNi_{100-x-y}$ composition-spread thin films and performed the combi-MOKE experiment with them. Figures 3e, 3f and 3g show the composition gradients of $Fe_xCo_yIr_{100-x-y}$, $Fe_xCo_yPt_{100-x-y}$ and $Fe_xCo_yNi_{100-x-y}$ composition-spread thin films. All of the MOKE curves are shown in Supplementary Fig. S3. In addition to the combi-MOKE experiments, we also carried out combinatorial X-ray diffraction (combi-XRD) experiments to investigate the crystal structure³⁹ and confirmed that all the materials are non-epitaxial films with bcc structure. All of the XRD curves are also shown in Supplementary Fig. S4.

Figures 3h, 3i and 3j show M_{MOKE} colour maps of $Fe_xCo_yIr_{100-x-y}$, $Fe_xCo_yPt_{100-x-y}$ and $Fe_xCo_yNi_{100-x-y}$, respectively. It was found that small amounts of Ir and Pt impurities enhance the M_{MOKE} , while Ni impurity monotonically decreases the M_{MOKE} . To clarify this, Fig. 3k shows M_{MOKE} of $(Fe_{75.2}Co_{24.8})_{1-x}Ir_x$, $(Fe_{75.3}Co_{24.7})_{1-x}Pt_x$ and $(Fe_{71.1}Co_{28.9})_{1-x}Ni_x$ along dotted arrows in Figs. 3h, 3i and 3j, respectively. The dark-blue solid line and blue dotted line in Fig. 3k show theoretical M_{MOKE} values of pure Fe ($M_{MOKE}^{Fe} = \frac{m_{Fe}}{m_{Fe}} = 1$) and $Fe_{75}Co_{25}$ ($M_{MOKE}^{FeCo} = \frac{m_{Fe_{75}Co_{25}}}{m_{Fe}} \approx 1.136$), where m_{Fe} and $m_{Fe_{75}Co_{25}}$ are magnetic moments of Fe and $Fe_{75}Co_{25}$, respectively. It is clearly seen that the $(Fe_{75.2}Co_{24.8})_{1-x}Ir_x$ exhibit large M_{MOKE} beyond M_{MOKE}^{FeCo} .

Similar results were also obtained by another experiment, a superconducting quantum interference device (SQUID)⁴¹ experiment. Figure 3l shows magnetization curves of $Fe_{73.2}Co_{24.2}Ir_{2.6}$ (whose M_{MOKE} is the

1 largest in Fig. 3h), $\text{Fe}_{84.0}\text{Co}_{12.0}\text{Pt}_{4.0}$ (whose M_{MOKE} is the largest in Fig. 3i), $\text{Fe}_{75.2}\text{Co}_{24.8}$, and pure Fe at room
2 temperature ($T = 300$ K). As with the case of the MOKE experiments, the magnetic field is applied along an in-
3 plane direction, and the vertical axis value is normalized by maximum SQUID intensity (emu/cc) of pure Fe. It is
4 clearly seen that inserting Ir and Pt impurity into FeCo alloy enhances magnetization. Figure 3m shows the
5 results of SQUID experiments at a low temperature ($T = 5$ K). As at room temperature, we can see clear
6 enhancement of magnetization by Ir and Pt impurities.

7 In addition to the two experimental confirmations, theoretical confirmation by ab-initio simulation (KKR-
8 CPA) was also conducted. Figures 4a, 4b and 4c show ternary plots of magnetic moment of $\text{Fe}_x\text{Co}_y\text{Ir}_{100-x-y}$.
9 $\text{Fe}_x\text{Co}_y\text{Pt}_{100-x-y}$ and $\text{Fe}_x\text{Co}_y\text{Ni}_{100-x-y}$, respectively. Small amounts of Ir and Pt impurities enhance magnetic moment
10 in $\text{Fe}_x\text{Co}_y\text{Ir}_{100-x-y}$ and $\text{Fe}_x\text{Co}_y\text{Pt}_{100-x-y}$ systems. On the other hand, increasing amounts of Ni monotonically
11 decrease magnetic moment in the $\text{Fe}_x\text{Co}_y\text{Ni}_{100-x-y}$ system. These results are consistent with the results of MOKE
12 and SQUID experiments.

13 Discussion

14 These experimental and theoretical results confirmed that the autonomous materials search system
15 had discovered materials that had previously never been considered. Moreover, the discovery of novel materials
16 can stimulate further theoretical studies. In this case, the materials found by the autonomous system led to a
17 theoretical investigation of why these impurities (Ir and Pt) enhance the magnetization.

18 Figures 5a and 5b show the ab-initio simulation results of local magnetic moments of Fe and Co in the
19 ternary alloy $\text{Fe}_{75}\text{Co}_{25}\text{X}_1$, where impurity X is a transition metal. Several elements around Ir and Pt in the periodic
20 table increase the Fe and Co local magnetic moments. Figure 5c shows the lattice constant, which is thought to

1 be one of the key parameters determining how the magnetic moment behaves in the $\text{Fe}_{75}\text{Co}_{25}\text{X}_1$ ternary alloys.
2 Comparing Figs. 5a, 5b and 5c, one finds that not all elements that expand the lattice constant increase the Fe
3 and Co local magnetic moments: Ta does not increase them even though $\text{Fe}_{75}\text{Co}_{25}\text{Ta}_1$ has a large lattice
4 constant. Figure 5e shows the local magnetic moments of the X elements in $\text{Fe}_{75}\text{Co}_{25}\text{X}_1$ ternary alloys.
5 Paramagnetic elements have much smaller local magnetic moments than ferromagnetic elements.

6 Our inductive theoretical study revealed that the $\text{Fe}_x\text{Co}_y\text{Ir}_{100-x-y}$ and $\text{Fe}_x\text{Co}_y\text{Pt}_{100-x-y}$ alloys have very high
7 magnetization because Ir and Pt impurities enhance the local magnetic moments of Fe and Co. However, too
8 much Ir and Pt in the alloy reduces the magnetization because their local magnetic moments are small.
9 Consequently, we observe the peaks of the $\text{Fe}_x\text{Co}_y\text{Ir}_{100-x-y}$ and $\text{Fe}_x\text{Co}_y\text{Pt}_{100-x-y}$ magnetization (magnetic moments)
10 in the heat maps (Figs. 3h, 3i, 4a and 4b). This new knowledge, that Ir and Pt impurities enhance local magnetic
11 moment of Fe and Co, will contribute to the development of materials for even stronger magnets. Thus, the
12 finding of an unexpected new material by the autonomous materials search system will promote further
13 experimental and/or theoretical studies.

14 In summary, stable alloys $\text{Fe}_x\text{Co}_y\text{Ir}_{100-x-y}$ and $\text{Fe}_x\text{Co}_y\text{Pt}_{100-x-y}$ with high magnetization beyond that of
15 Fe_3Co_1 were discovered via autonomous materials search system combining ML and *ab-initio* calculation. The
16 performance of these alloys was confirmed by both experiments and theories. These alloys can be used for
17 various applications, such as information storages, motors, sensors, actuators, and other electric devices. In
18 addition, our inductive theoretical study based on the data-driven materials discovery revealed that the Ir and Pt
19 impurities enhance the local magnetic moments of Fe and Co. This new knowledge has a potential to contribute
20 to the development of materials for even stronger magnets. Our autonomous system for materials discovery is

1 quite versatile and can be used in the development of various materials by selecting appropriate objective
2 properties and algorithms to be used in the virtual materials evaluation step and the next target
3 composition/structure decision step. We believe that use of this autonomous system will lead to the emergence
4 of more and more innovative materials and theories.

5

6 **Methods**

7 **Game tree search.** The game tree search algorithm³¹ is used to calculate the priority P of a candidate next
8 sampling point (composition). It tunes the trade-off between exploration and exploitation in the material search
9 space, which in this case is an eight-dimensional space composed of the a, b, c, d, e, f, g, and h composition
10 axes for the alloy $\text{Fe}_a\text{Co}_b\text{Ni}_c\text{Ru}_d\text{Rh}_e\text{Pd}_f\text{Ir}_g\text{Pt}_h$. The magnitude of the exploration is mathematically expressed as
11 an expected uncertainty σ , which tends to be large at sparse points in the search space. The magnitude of
12 exploitation is an expected value μ predicted on the basis of accumulated data. Both σ and μ are calculated
13 using a Gaussian process regression model in which the objective variable and explanatory variables are
14 respectively the total magnetic moment and the compositions (a, b, c, d, e, f, g, and h). To calculate the priority
15 of a candidate next sampling point, we use an upper confidence bound (UCB) strategy⁴² expressed as

$$16 \quad P = \sigma + C\mu. \quad (1)$$

17 Parameter C is used to tune the trade-off between exploration and exploitation. The cost of calculating P over
18 the entire eight-dimensional materials search space is reduced by using a tree structure for the game tree
19 search so that the spatial resolution increases stepwisely. The shallow part of the tree manages coarse-
20 composition spatial resolution while the deep part manages fine-composition spatial resolution. Error pruning is

1 used to exclude from the set of candidate next sampling points those with σ lower than threshold e_{\min} . In this
2 study, parameter C in the UCB formula (Eq. 1), initial spatial resolution d_0 , tree depth D , and threshold e_{\min} were
3 set to 0.3, 0.8, 13, and 0.0001, respectively³¹.

4 **KKR-CPA.** The Korringa–Kohn–Rostoker coherent potential approximation³² is a Green’s function-based density
5 functional theory calculation often used for disordered multicomponent alloys. Based on first-principles theory, it
6 can predict various material properties, including the magnetic moment, from composition and crystal structure
7 data. In this study we used AkaiKKR software³². The crystal structural type (“brvtyp”) was set to bcc. Lattice
8 constant a between 5.27 and 5.38 bohr was optimized by minimizing the total energy. An imaginary part at the
9 Fermi level (“edelt”) and the width of the energy contour were set to 0.001 Ry and 1.0 Ry, respectively. When
10 calculating the magnetic moments in the FeCoX systems shown in Figs. 4, we set the relativistic treatment type
11 (“reltyp”) to “srals” including both the relativistic effect and spin-orbit interaction effect. In the KKR-CPA
12 calculation for the autonomous materials search system shown in Fig. 2, the “reltyp” was set to “nrl”, which
13 means no relativistic effect or spin-orbit interaction effect, in order to reduce calculation cost. The “bzqlty”
14 parameter, which specifies the quality of the Brillouin zone mesh, was set to 9. The maximum angular
15 momentum taken into account (“xml”) was 3.

16 **Limitation of the material search space.** Ideally, the search for a material with a large magnetic moment would
17 take place in a very large search space with axes for all metallic elements, but this is not feasible due to the
18 computational cost and KKR-CPA performance limitation. There are more than 50 metallic elements in the
19 periodic table, which is too large a number for KKR-CPA to converge in the AkaiKKR software³². We therefore
20 performed some calculation by hand beforehand. We calculated the local magnetic moments of various

1 impurities in Fe, which is the likely main element in an alloy with a large magnetic moment. Supplementary Fig.
2 S1 shows the KKR-CPA results for the local magnetic moment of various impurities (X) in Fe_{99}X_1 with a bcc
3 structure. We identified eight elements (Fe, Co, Ni, Ru, Rh, Pd, Ir and Pt) that have local magnetic moments
4 greater than $+0.25 \mu_B$. Because conventional materials simulation technologies (KKR-CPA in this case) are also
5 being advanced, we should be able to simulate alloys with more components in the future. And in an expanded
6 search space, the autonomous system might discover an alloy with even better properties.

7 **Combinatorial experiment.** To fabricate composition-spread thin film of $\text{Fe}_x\text{Co}_y\text{Ir}_{100-x-y}$, $\text{Fe}_x\text{Co}_y\text{Pt}_{100-x-y}$ and
8 $\text{Fe}_x\text{Co}_y\text{Ni}_{100-x-y}$ on a SiO_2/Si substrate, we employ a combinatorial sputtering system³⁶⁻³⁹. Using the moving mask
9 motion, very thin unit layers with wedge shaped thickness are deposited and stacked alternately³⁸. Because
10 the thicknesses of the unit layers are about 0.2 nm, which is almost equal to the atomic distance, the ideal
11 material mixtures can be obtained by using a post-deposition annealing process. We used a combinatorial
12 sputtering system (CMS-6400)³⁸, whose ultimate vacuum is at 3×10^{-6} Pa. Sputtering using Fe, Ir, Pt and Ni
13 metal targets was done with a radio-frequency (RF) source, while that using a Co metal target was done with a
14 direct current (DC) source. The alternative sputtering deposition was carried out under an Ar atmosphere (40
15 sccm, 0.3 Pa) at room temperature. The total thickness of the thin films was 100 nm. After deposition, films were
16 annealed at 600 °C in vacuum (3×10^{-5} Pa) for 1 hour. On the composition-spread sample, we carried out
17 combinatorial longitudinal magneto-optic Kerr effect (combi-MOKE)³⁹ experiments at room temperature. To
18 detect magneto-optical Kerr rotations (MOKE intensity), a magnetic field ranging from -650 Oe to +650 Oe was
19 applied in an in-plane direction. Sampling distances on the composition thin film were 2 mm and 3.3 mm for the
20 x and y directions, respectively, as shown in Fig. 3b. After the combi-MOKE experiments, the composition-

1 spread samples were cut into small tips (2 mm × 3.3 mm) by using the dicing machine for a superconducting
2 quantum interference device (SQUID)⁴¹ experiment. Lowering the temperature to 5 K was done by field cooling.
3 To obtain magnetization curves, a magnetic field ranging from −400 Oe to +400 Oe was applied in an in-plane
4 direction.

5 **Data availability.** The data and code that support the results reported in this paper and other findings of this
6 study are available from the corresponding author upon reasonable request.

8 **Acknowledgements**

9 We thank S. Ri in Comet Inc. for combinatorial experiments and thank I. Takeuchi and V. Stanev in the University
10 of Maryland and M. Kotsugi in Tokyo University of Science for valuable discussion. This work was supported by
11 JST-PRESTO under the “Advanced Materials Informatics through Comprehensive Integration among
12 Theoretical, Experimental, Computational and Data-Centric Sciences” research area (Grant JPMJPR17N4) and
13 by the JST-ERATO “Spin Quantum Rectification Project” (Grant JPMJER1402).

15 **Author contributions**

16 Y.I., R.S. and M.I. contributed to the theoretical discussion and the machine learning algorithm discussion. Y.I.
17 wrote the manuscript. E.S. and M.I supervised the study. All the authors discussed the results and commented
18 on the manuscript.

1 **Competing interest declaration**

2 The authors declare no competing interests.

3

4 **References**

5 1. Spaldin, N. A. *Magnetic Materials: Fundamentals and Applications* (Cambridge University Press, Cambridge,
6 2010).

7 2. Gutfleisch, O. *et al.* Magnetic materials and devices for the 21st century: stronger, lighter, and more energy
8 efficient. *Adv. Mater.* **23**, 821–842 (2011).

9 3. Li, D., Li, Y., Pan, D., Zhang, Z., & Choi, C-J. Prospect and status of iron-based rare-earth-free permanent
10 magnetic materials. *J. Magn. Magn. Mater.* **469**, 535–544 (2019).

11 4. Cui, J. *et al.* Current progress and future challenges in rare-earth-free permanent magnets. *Acta Mater.* **158**,
12 118–137 (2018).

13 5. Snow, R. J., Bhatkar, H., N'Diaye, A. T., Arenholz, E. & Idzerda, Y. U. Large moments in bcc Fe_xCo_yMn_z
14 ternary alloy thin films. *Appl. Phys. Lett.* **112**, 7 (2018)

15 6. Kakehashi, Y. *Modern Theory of Magnetism in Metals and Alloys* (Springer-Verlag, Berlin Heidelberg, 2012).

16 7. Butler, K. T., Davies, D. W., Cartwright, H., Isayev, O. & Walsh, A. Machine learning for molecular and
17 materials science. *Nature* **559**, 547–555 (2018).

18 8. Mueller, T., Kusne, A. G. & Ramprasad, R. Machine learning in material science: recent progress and
19 emerging applications. *Rev. Comput. Chem.* **29**, 186–273 (2016).

20 9. Jose, R. & Ramakrishna, S. Materials 4.0: Materials big data enabled materials discovery. *Appl. Mater. Today*

1 **10**, 127–132 (2018).

2 10. Senderowitz, H. & Tropsha, A. Materials informatics. *J. Chem. Inf. Model.* **58**, 2377–2379 (2018).

3 11. Ramprasad, R., Batra, R., Pilia, G., Mannodi-Kanakkithodi, A. & Kim, C. Machine learning in materials
4 informatics: recent applications and prospects. *npj Comput. Mater.* **3**, 54 (2017).

5 12. Agrawal, A. & Choudhary, A. Perspective: Materials informatics and big data: realization of the ‘fourth
6 paradigm’ of science in materials science. *APL Mater.* **4**, 053208 (2016).

7 13. Lookman, T., Alexander, F. J. & Rajan, K. *Information Science for Materials Discovery and Design* (Springer,
8 Switzerland, 2016).

9 14. Raccuglia, P. *et al.* Machine-learning-assisted materials discovery using failed experiments. *Nature* **553**, 73–
10 77 (2016).

11 15. Lookman, T., Eidenbenz, S., Alexander, F. & Barnes, C. (eds) *Materials Discovery and Design by Means of*
12 *Data Science and Optimal Learning* (Springer International Publishing, Basel, 2018).

13 16. Schmidt, J., Marques, M. R. G., Botti S. & Marques, M. A. L. Recent advances and applications of machine
14 learning in solid-state materials science. *npj Comput. Mater.* **5**, 83 (2019).

15 17. Burger, B. *et al.* A mobile robotic chemist. *Nature* **583**, 237-241 (2020).

16 18. Kusne, A. G. *et al.* On-the-fly machine-learning for high-throughput experiments: search for rare-earth-free
17 permanent magnets. *Sci. Rep.* **4**, 6367 (2014).

18 19. Halder, A., Ghosh, A. & Dasgupta, T. S. Machine-learning-assisted prediction of magnetic double
19 perovskites. *Phys. Rev. Materials* **3**, 084418 (2019).

20 20. Sodeyama, K., Igarashi, Y., Nakayama, T., Tateyama, Y. & Okara, M. Liquid electrolyte informatics using an

- 1 exhaustive search with linear regression. *Phys. Chem. Chem. Phys.* **20**, 22585–22591 (2018).
- 2 21. Wu, B., Han, S., Shin, K. G. & Lu, W. Application of artificial neural networks in design of lithium-ion
3 batteries. *J. Power Sources* **395**, 128–136 (2018).
- 4 22. Stanev, V. *et al.* Machine learning modeling of superconducting critical temperature. *npj Comput. Mater.* **4**,
5 29 (2018).
- 6 23. Ishikawa, T., Miyake, T. & Shimizu, K. Materials informatics based on evolutionary algorithms: Application to
7 search for superconducting hydrogen compounds. *Phys. Rev. B* **100**, 174506 (2019).
- 8 24. Balachandran, P. V., Young, J., Lookman, T. & Rondinelli, J. M. Learning from data to design functional
9 materials without inversion symmetry. *Nat. Commun.* **8**, 14282 (2017).
- 10 25. Balachandran, P. V., Kowalski, B., Sehirlioglu, A. & Lookman, T. Experimental search for high-temperature
11 ferroelectric perovskites guided by two-step machine learning. *Nat. Commun.* **9**, 1668 (2018).
- 12 26. Iwasaki, Y. *et al.* Identification of advanced spin-driven thermoelectric materials via interpretable machine
13 learning. *npj Comput. Mater.* **5**, 103 (2019).
- 14 27 Iwasaki, Y. *et al.* Machine-learning guided discovery of a new thermoelectric material. *Sci. Rep.* **9**, 2751
15 (2019).
- 16 28. Ishida, N., Wakamiya, A. & Saeki, A. Quantifying hole transfer yield from perovskite to polymer layer:
17 statistical correlation of solar cell outputs with kinetic and energetic properties. *ACS Photonics* **3**, 1678–1688
18 (2016).
- 19 29. Takahashi, K., Takahashi, L., Miyazato, I. and Tanaka, Y. Searching for hidden perovskite materials for
20 photovoltaic systems by combining data science and first principle calculations. *ACS Photonics* **5**, 771–775

1 (2018).

2 30. Sumita, M., Yang, X., Ishihara, S., Tamura, R. & Tsuda, K. Hunting for organic molecules with artificial
3 intelligence: molecules optimized for desired excitation energies. *ACS Cent. Sci.* **4**, 1126–1133 (2018).

4 31. Sawada, R., Iwasaki, Y. & Ishida, M. Boosting material modeling using game tree search. *Phys. Rev. Mater.*
5 **2**, 103802 (2018).

6 32. Akai, H. Electronic structure Ni-Pd alloys calculated by the self-consistent KKR-CPA method. *J. Phys. Soc.*
7 *Jpn.* **51**, 468–474 (1982).

8 33. Khan, N. S., Staunton, J. B., & Stocks, G. M. Statistical physics of multicomponent alloys using KKR-CPA.
9 *Phys. Rev. B* **93**, 054206 (2016).

10 34. Yang, L. *et al.* Investigation of the site preference in Mn₂RuSn using KKR-CPA-LDA calculation. *J. Magn.*
11 *Magn. Mater.* **382**, 247–251 (2015).

12 35. Jin, K. *et al.* Tailoring the physical properties of Ni-based single-phase equiatomic alloys by modifying the
13 chemical complexity. *Sci. Rep.* **6**, 20159 (2016).

14 36. Koinuma, H. & Takeuchi, I. Combinatorial solid-state chemistry of inorganic materials. *Nat. Mater.* **3**, 429
15 (2004).

16 37. Takeuchi, I. *et al.* Identification of novel compositions of ferromagnetic shape-memory alloys using
17 composition spreads. *Nat. Mater.* **2**, 180–184 (2003).

18 38. Combinatorial Technology, Comet Inc. <https://www.comet-nht.com/concept-e.html>

19 39. Yoo, Y. K. *et al.* Identification of amorphous phases in the Fe-Ni-Co ternary alloy system using continuous
20 phase diagram material chips. *Intermetallics* **14**, 241–247 (2006).

- 1 40. Higo, T. *et al.* Large magneto-optical Kerr effect and imaging of magnetic octupole domains in an
2 antiferromagnetic metal. *Nat. Photon.* **12**, 73–78 (2018).
- 3 41. Clarke, J. & Braginski, A. I. *The SQUID Handbook: Applications of SQUIDs and SQUID Systems.* (John
4 Wiley & Sons, New York, 2006).
- 5 42. Auer, P. Using confidence bounds for exploitation-exploration trade-offs. *J. Mach. Learn. Res.* **3**, 397–422
6 (2002).

7
8
9
10
11
12
13
14
15
16
17
18
19

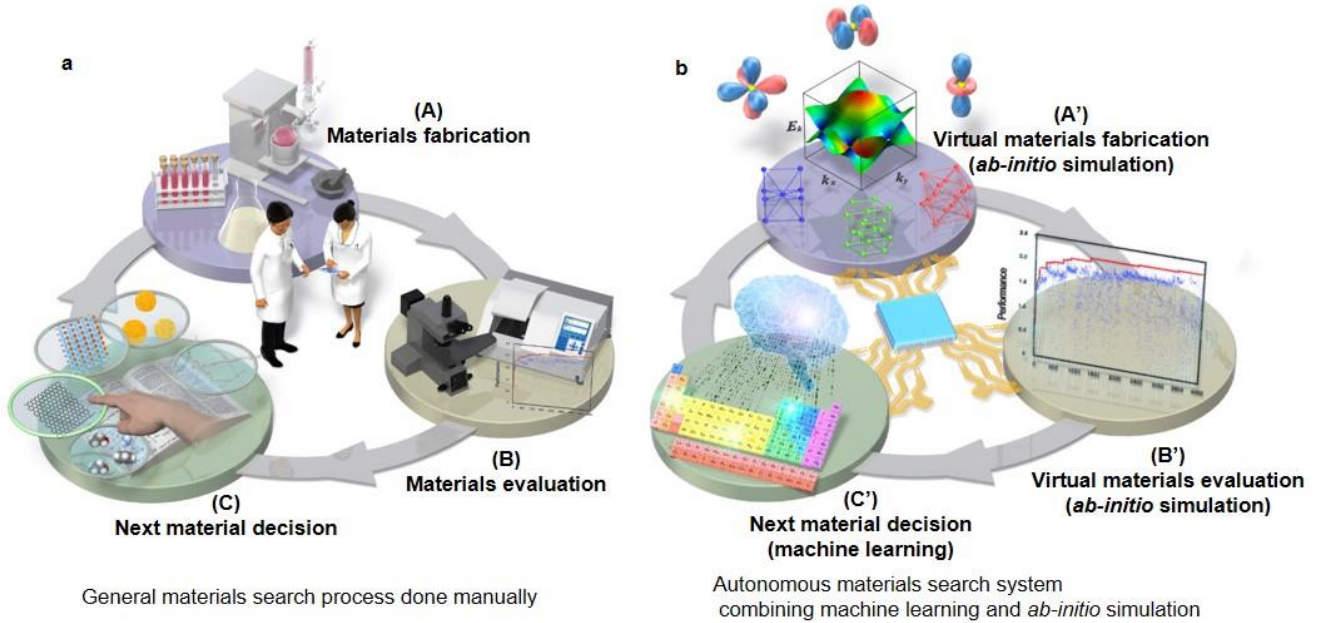


Fig. 1 | Concept of autonomous materials search system. a, Conventional materials search process done manually following a cycle comprising (A) a materials fabrication step, (B) a materials evaluation step, and (C) a decision step for selecting the next target material. **b**, Autonomous materials search system in which the conventional process of materials search is simulated using computation technologies including *ab-initio* simulation and machine learning (ML). The virtual materials fabrication step (A') and virtual materials evaluation step (B') are simulated using *ab-initio* simulation. The decision step for the next target material (C') is simulated using machine learning such as the game tree algorithm. This autonomous system automatically grows smarter as the amount of data acquired during the automated development cycle increases and eventually it finds a better material.

1
2
3
4
5
6
7
8
9
10
11
12
13

Figure 2

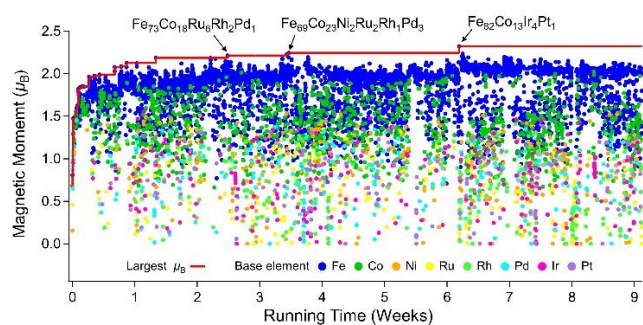
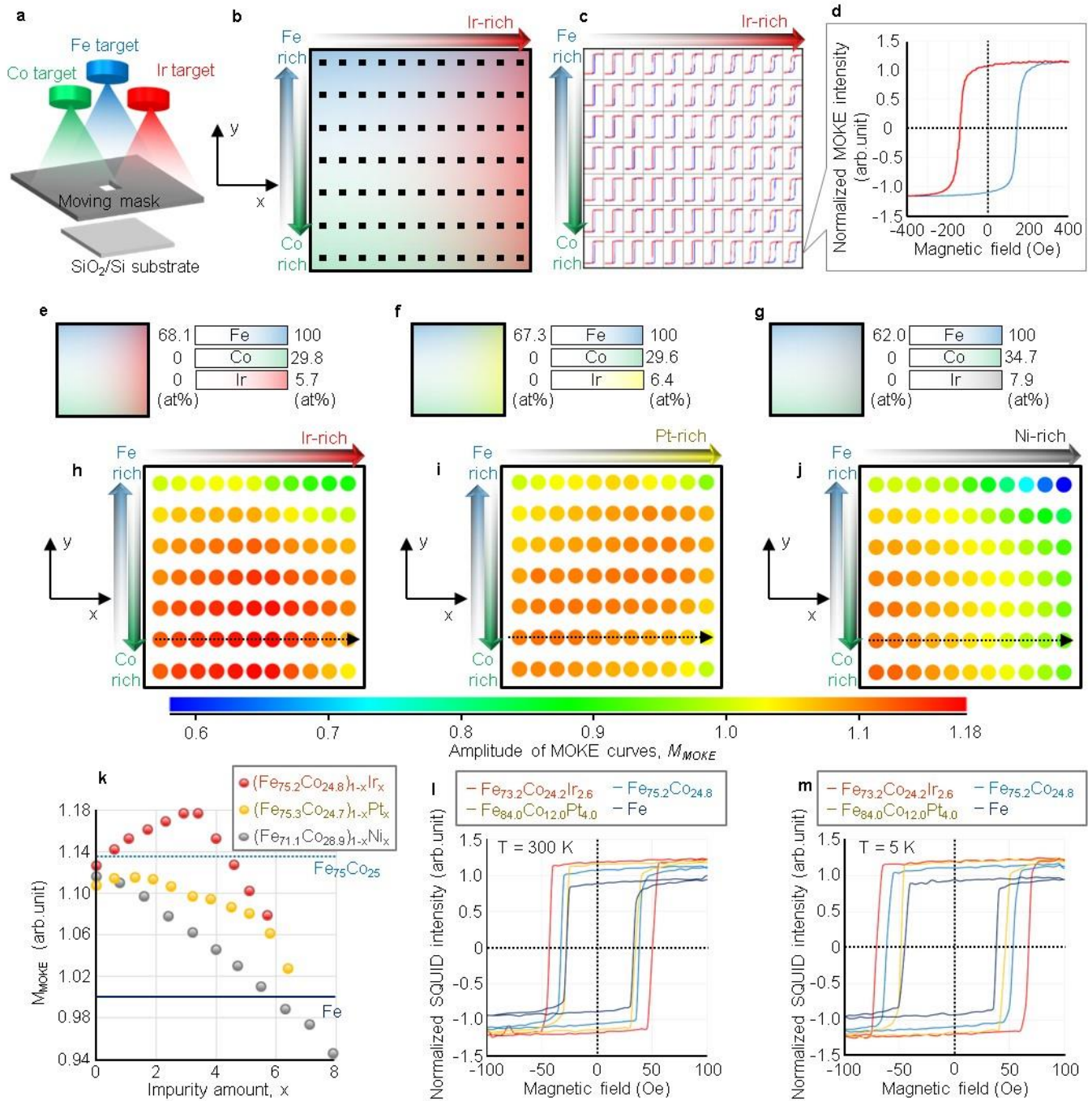


Fig. 2 | Growth of autonomous materials search system. Growth of the autonomous materials search system for an alloy with a large magnetic moment. Magnetic moment data were plotted for each search cycle shown in Fig. 1b. Colors of data points show the base element of the alloys. After some time, the autonomous system was able to find a better composition for a disordered multi-element alloy ($Fe_aCo_bNi_cRu_dRh_ePd_fIr_gPt_h$) with a large magnetic moment due to an increase in the amount of data for learning. After six weeks (strictly, 43 days) of growth, the autonomous system arrived at $Fe_{82}Co_{13}Ir_4Pt_1$, not the composition of the alloy at the top of the Slater–Pauling curve ($Fe_{75}Co_{25}$).

1

2 **Figure 3**

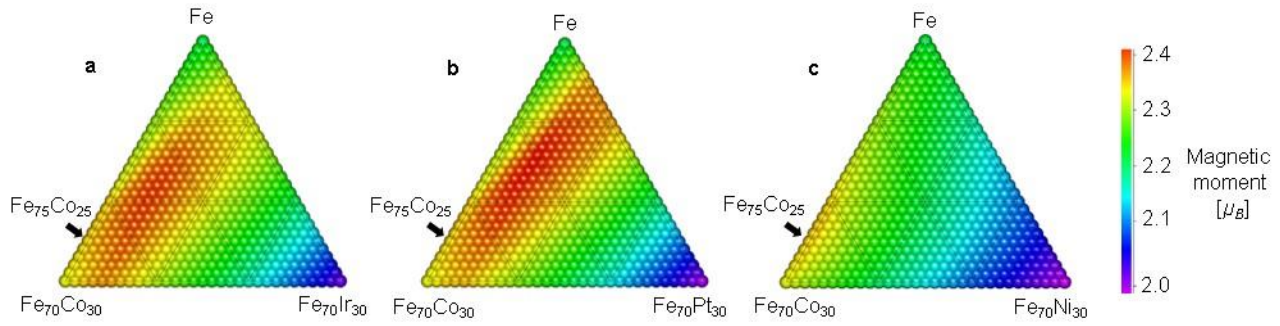
3

4 **Fig. 3 | Experimental confirmation by combinatorial MOKE and SQUID experiments. a, Illustration of**5 **combinatorial sputtering system with an automated moving mask for synthesizing $\text{Fe}_x\text{Co}_y\text{Ir}_{100-x-y}$, $\text{Fe}_x\text{Co}_y\text{Pt}_{100-x-y}$** 6 **and $\text{Fe}_x\text{Co}_y\text{Ni}_{100-x-y}$ composition-spread thin films on SiO_2/Si substrates. b, Composition map of $\text{Fe}_x\text{Co}_y\text{Ir}_{100-x-y}$**

1 composition-spread thin film, where the Ir composition gradient is along the X direction, and Fe and Co
2 composition gradients are along opposite Y directions. The black spots denote sampling points of the combi-
3 MOKE experiments. **c**, Results of combi-MOKE experiments with $\text{Fe}_x\text{Co}_y\text{Ir}_{100-x-y}$ composition-spread sample. **d**,
4 MOKE curves of $\text{Fe}_{68.1}\text{Co}_{26.2}\text{Ir}_{5.7}$ (bottom right point in Fig. 3b). **e, f, g**, Composition maps of $\text{Fe}_x\text{Co}_y\text{Ir}_{100-x-y}$,
5 $\text{Fe}_x\text{Co}_y\text{Pt}_{100-x-y}$ and $\text{Fe}_x\text{Co}_y\text{Ni}_{100-x-y}$ composition-spread thin films, respectively. **h, i, j**, Mapping of amplitude of
6 MOKE curves M_{MOKE} (\propto saturation magnetization M_s) of the $\text{Fe}_x\text{Co}_y\text{Ir}_{100-x-y}$, $\text{Fe}_x\text{Co}_y\text{Pt}_{100-x-y}$ and $\text{Fe}_x\text{Co}_y\text{Ni}_{100-x-y}$
7 composition-spread thin films, respectively. Small amounts of Ir and Pt impurities enhance the M_{MOKE} , while Ni
8 impurity monotonically decreases the M_{MOKE} . **k**, M_{MOKE} plots of $(\text{Fe}_{75.2}\text{Co}_{24.8})_{1-x}\text{Ir}_x$, $(\text{Fe}_{75.3}\text{Co}_{24.7})_{1-x}\text{Pt}_x$ and
9 $(\text{Fe}_{71.1}\text{Co}_{28.9})_{1-x}\text{Ni}_x$ along dotted arrows in Figs. 3h, 3i and 3j, respectively. The dark-blue solid line and blue
10 dotted line show theoretical M_{MOKE} values of pure Fe and $\text{Fe}_{75}\text{Co}_{25}$, respectively. **l, m**, Magnetization curves
11 obtained in SQUID experiments with $\text{Fe}_{73.2}\text{Co}_{24.2}\text{Ir}_{2.6}$, $\text{Fe}_{84.0}\text{Co}_{12.0}\text{Pt}_{4.0}$, $\text{Fe}_{75.2}\text{Co}_{24.8}$ and pure Fe at room
12 temperature ($T = 300$ K) and low temperature ($T = 5$ K). The magnetization enhancement due to Ir and Pt
13 impurities were also observed in the SQUID experiments.

1

2 **Figure 4**



3

4 **Fig. 4 | Theoretical confirmation by ab-initio simulation.** To confirm and analyse the novel alloy discovered

5 by the autonomous materials search system and combinatorial experiments, the magnetic moments in various

6 ternary alloys were investigated by *ab-initio* calculation. **a**, Magnetic moments in FeCoIr ternary alloy system

7 (largest magnetic moment was observed for $\text{Fe}_{81}\text{Co}_{15}\text{Ir}_4$). **b**, Magnetic moments in FeCoPt ternary alloy system

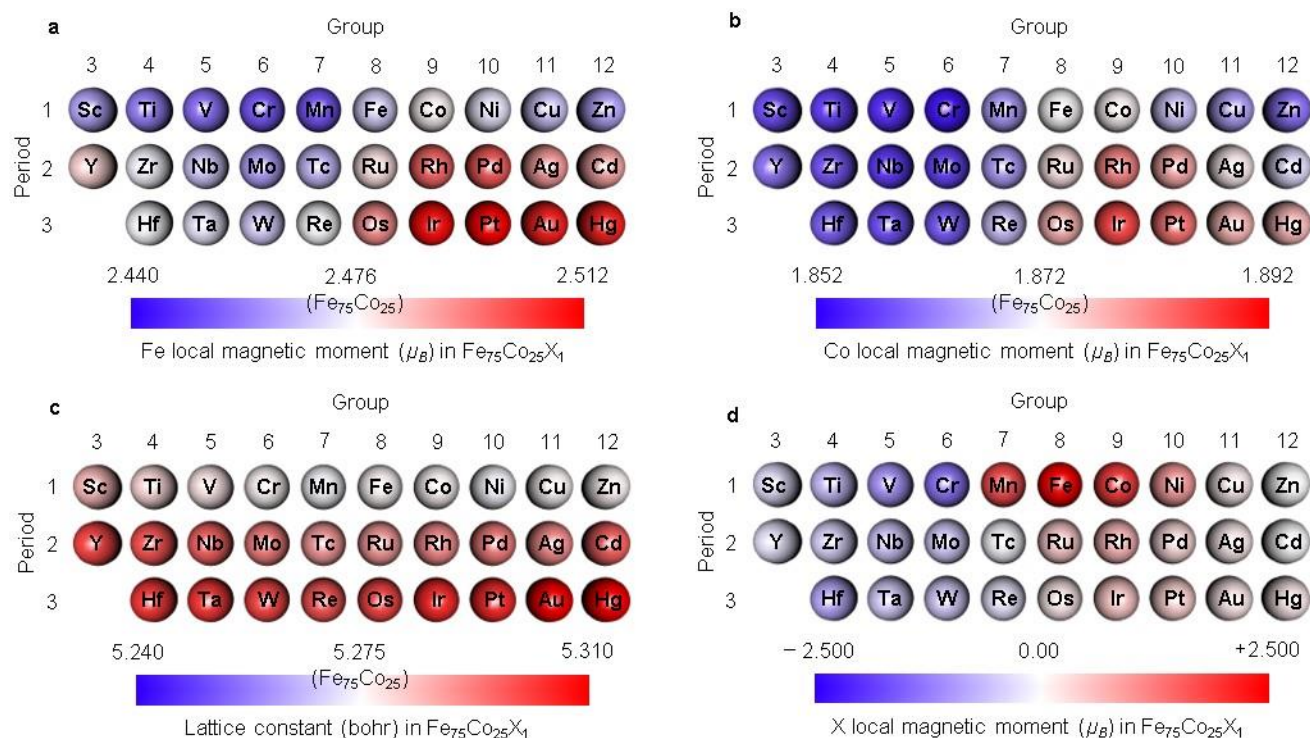
8 (largest magnetic moment was observed for $\text{Fe}_{85}\text{Co}_{11}\text{Pt}_4$). **c**, Magnetic moments in FeCoNi ternary alloy system

9 (Ni impurities do not enhance magnetic moment, so the largest magnetic moment was observed in the alloy at

10 the top of the Slater–Pauling curve, $\text{Fe}_{75}\text{Co}_{25}$).

11

1 **Figure 5**



2

3

4 **Fig. 5 | Theoretical analysis by ab-initio simulation. a**, Fe local magnetic moment in the $\text{Fe}_{75}\text{Co}_{25}\text{X}_1$ system,

5 where X is a transition metal. The centre of the colour bar (white part) corresponds to the Fe local magnetic

6 moment in $\text{Fe}_{75}\text{Co}_{25}$. Ir and Pt (and other elements around them in the periodic table) enhance the Fe local

7 magnetic moment. **b**, Co local magnetic moment in the $\text{Fe}_{75}\text{Co}_{25}\text{X}_1$ system. Ir and Pt (and other elements around

8 them) also enhance the Co local magnetic moment. **c**, Lattice constant of the $\text{Fe}_{75}\text{Co}_{25}\text{X}_1$ system. Elements with

9 large atomic numbers tend to expand the lattice constant of $\text{Fe}_{75}\text{Co}_{25}$. **d**, Local magnetic moments of different X

10 elements in the $\text{Fe}_{75}\text{Co}_{25}\text{X}_1$ system. Positive and negative signs respectively mean parallel and anti-parallel

11 magnetic moments with respect to the Fe and Co local magnetic moments. Paramagnetic elements, including Ir

12 and Pt, have smaller magnetic moments than ferromagnetic elements (Fe, Co and Ni).

13

Figures

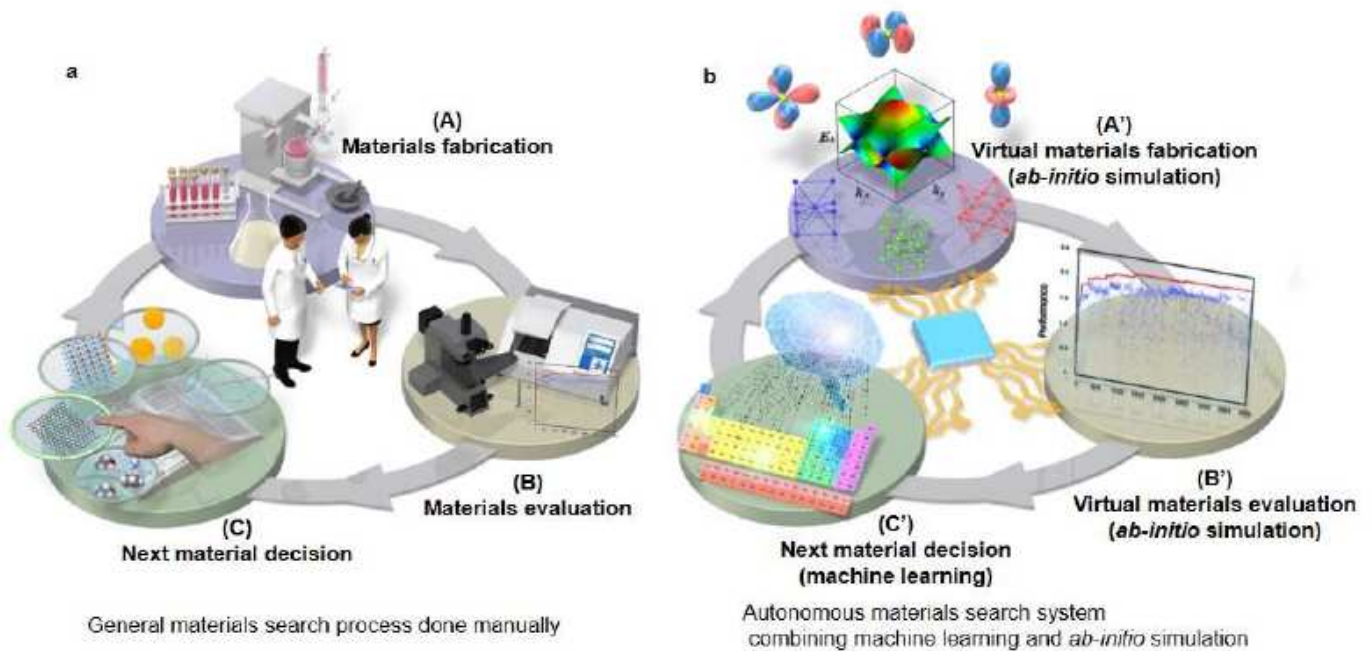


Figure 1

Concept of autonomous materials search system. a, Conventional materials search process done manually following a cycle comprising (A) a materials fabrication step, (B) a materials evaluation step, and (C) a decision step for selecting the next target material. b, Autonomous materials search system in which the conventional process of materials search is simulated using computation technologies including *ab-initio* simulation and machine learning (ML). The virtual materials fabrication step (A') and virtual materials evaluation step (B') are simulated using *ab-initio* simulation. The decision step for the next target material (C') is simulated using machine learning such as the game tree algorithm. This autonomous system automatically grows smarter as the amount of data acquired during the automated development cycle increases and eventually it finds a better material.

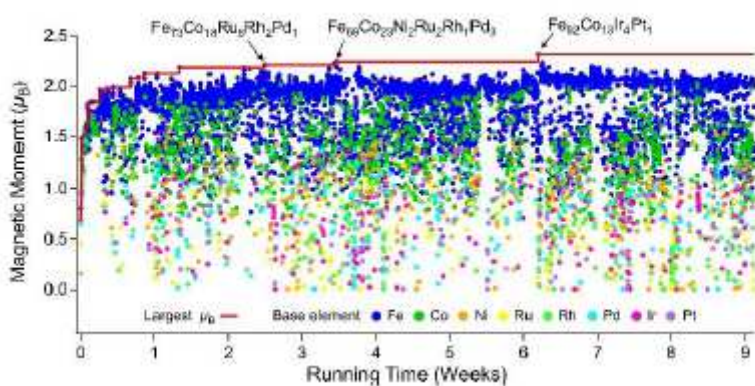


Figure 2

Growth of autonomous materials search system. Growth of the autonomous materials search system for an alloy with a large magnetic moment. Magnetic moment data were plotted for each search cycle shown in Fig. 1b. Colors of data points show the base element of the alloys. After some time, the autonomous system was able to find a better composition for a disordered multi-element alloy (FeCoNiCuPdRhIrPt) with a large magnetic moment due to an increase in the amount of data for learning. After six weeks (strictly, 43 days) of growth, the autonomous system arrived at Fe₈₂Co₁₃Ir₄Pt₁, not the composition of the alloy at the top of the Slater–Pauling curve

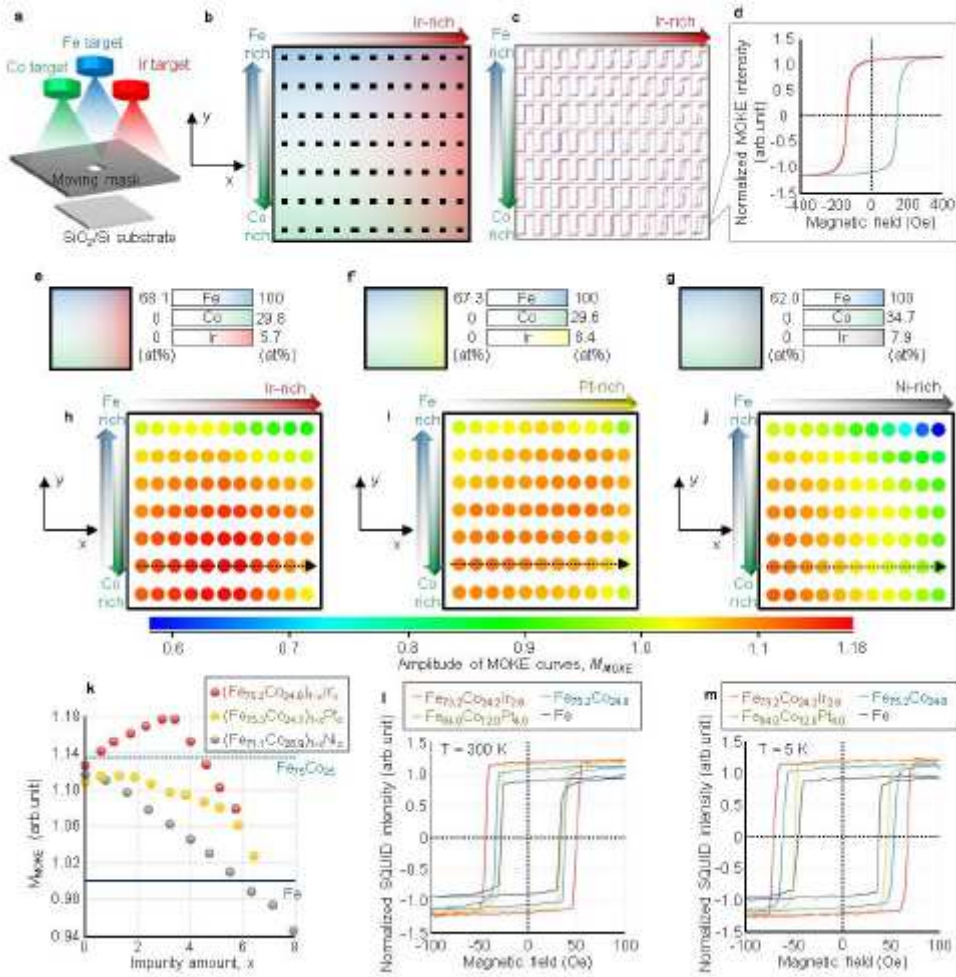


Figure 3

Experimental confirmation by combinatorial MOKE and SQUID experiments. a, Illustration of combinatorial sputtering system with an automated moving mask for synthesizing Fe_xCo_yIr_{100-x-y}, Fe_xCo_yPt_{100-x-y} and Fe_xCo_yNi_{100-x-y} composition-spread thin films on SiO₂/Si substrates. b, Composition map of Fe_xCo_yIr_{100-x-y} composition-spread thin film, where the Ir composition gradient is along the X direction, and Fe and Co 1 composition gradients are along opposite Y directions. The black spots denote sampling points of the combi-2 MOKE experiments. c, Results of combi-MOKE experiments with Fe_xCo_yIr_{100-x-y} composition-spread sample. d, MOKE curves of Fe_{68.1}Co_{26.2}Ir_{5.7} (bottom right point in Fig. 3b). e, f, g, Composition maps of Fe_xCo_yIr_{100-x-y}, Fe_xCo_yPt_{100-x-y} and Fe_xCo_yNi_{100-x-y}

composition-spread thin films, respectively. h, i, j, Mapping of amplitude of MOKE curves MMOKE (\propto saturation magnetization M_s) of the $\text{Fe}_x\text{Co}_y\text{Ir}_{100-x-y}$, $\text{Fe}_x\text{Co}_y\text{Pt}_{100-x-y}$ and $\text{Fe}_x\text{Co}_y\text{Ni}_{100-x-y}$ composition-spread thin films, respectively. Small amounts of Ir and Pt impurities enhance the MMOKE , while Ni impurity monotonically decreases the MMOKE . k, MMOKE plots of $(\text{Fe}_{75.2}\text{Co}_{24.8})_{1-x}\text{Ir}_x$, $(\text{Fe}_{75.3}\text{Co}_{24.7})_{1-x}\text{Pt}_x$ and $(\text{Fe}_{71.1}\text{Co}_{28.9})_{1-x}\text{Ni}_x$ along dotted arrows in Figs. 3h, 3i and 3j, respectively. The dark-blue solid line and blue dotted line show theoretical MMOKE values of pure Fe and $\text{Fe}_{75}\text{Co}_{25}$, respectively. l, m, Magnetization curves obtained in SQUID experiments with $\text{Fe}_{73.2}\text{Co}_{24.2}\text{Ir}_{2.6}$, $\text{Fe}_{84.0}\text{Co}_{12.0}\text{Pt}_{4.0}$, $\text{Fe}_{75.2}\text{Co}_{24.8}$ and pure Fe at room temperature ($T = 300$ K) and low temperature ($T = 5$ K). The magnetization enhancement due to Ir and Pt impurities were also observed in the SQUID experiments.

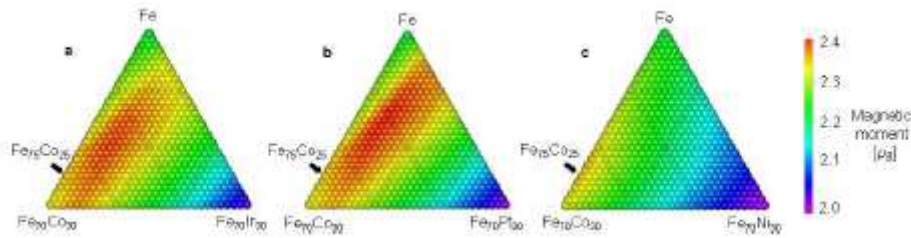


Figure 4

Theoretical confirmation by ab-initio simulation. To confirm and analyse the novel alloy discovered by the autonomous materials search system and combinatorial experiments, the magnetic moments in various ternary alloys were investigated by ab-initio calculation. a, Magnetic moments in FeCoIr ternary alloy system (largest magnetic moment was observed for $\text{Fe}_{81}\text{Co}_{15}\text{Ir}_4$). b, Magnetic moments in FeCoPt ternary alloy system (largest magnetic moment was observed for $\text{Fe}_{85}\text{Co}_{11}\text{Pt}_4$). c, Magnetic moments in FeCoNi ternary alloy system (Ni impurities do not enhance magnetic moment, so the largest magnetic moment was observed in the alloy at the top of the Slater–Pauling curve, $\text{Fe}_{75}\text{Co}_{25}$).

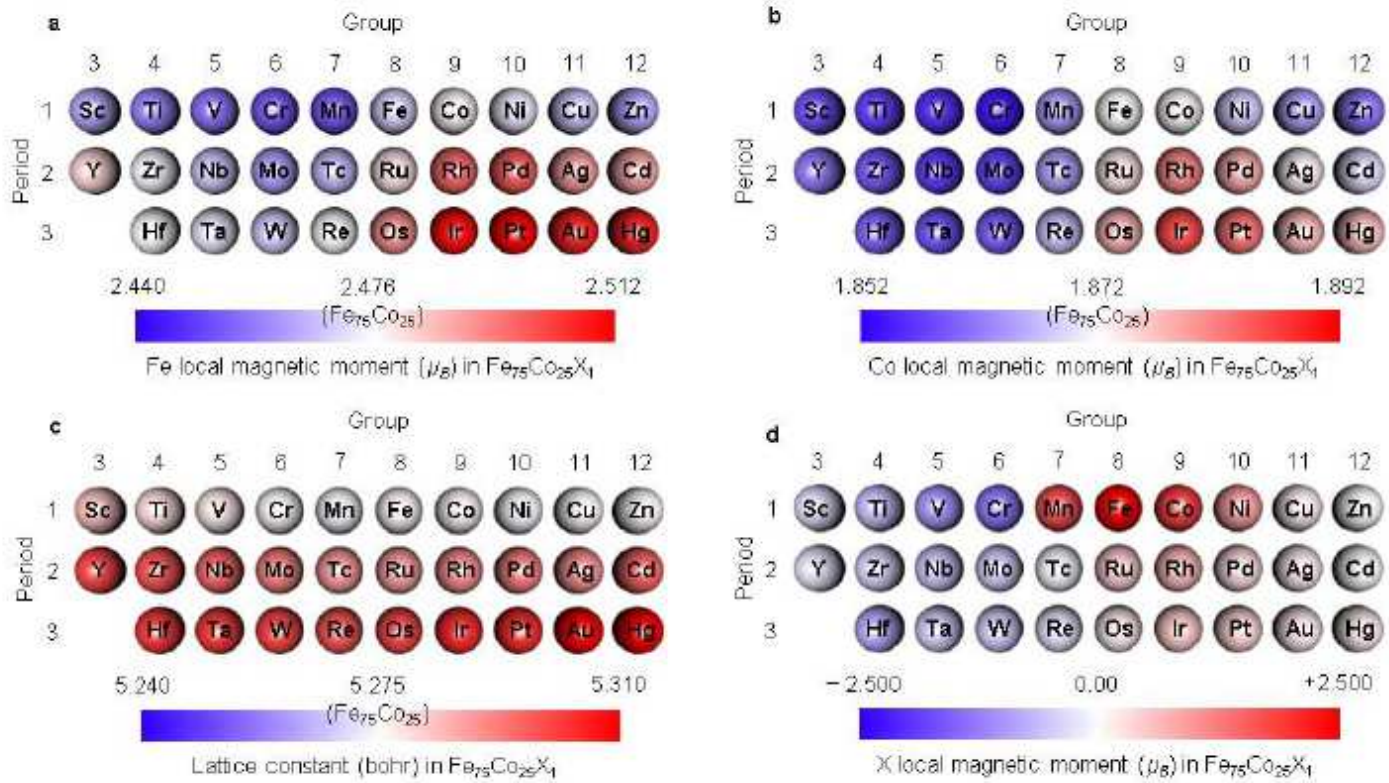


Figure 5

Theoretical analysis by ab-initio simulation. a, Fe local magnetic moment in the Fe75Co25X1 system, where X is a transition metal. The centre of the colour bar (white part) corresponds to the Fe local magnetic moment in Fe75Co25. Ir and Pt (and other elements around them in the periodic table) enhance the Fe local magnetic moment. b, Co local magnetic moment in the Fe75Co25X1 system. Ir and Pt (and other elements around them) also enhance the Co local magnetic moment. c, Lattice constant of the Fe75Co25X1 system. Elements with large atomic numbers tend to expand the lattice constant of Fe75Co25. d, Local magnetic moments of different X elements in the Fe75Co25X1 system. Positive and negative signs respectively mean parallel and anti-parallel magnetic moments with respect to the Fe and Co local magnetic moments. Paramagnetic elements, including Ir and Pt, have smaller magnetic moments than ferromagnetic elements (Fe, Co and Ni).

Supplementary Files

This is a list of supplementary files associated with this preprint. Click to download.

- [FigS1.png](#)
- [FigS2.png](#)
- [FigS3.png](#)
- [FigS4.png](#)